APL Machine Learning

RESEARCH ARTICLE | AUGUST 09 2024

Deep-learning design of electronic metasurfaces in graphene for quantum control and Dirac electron holography

Chen-Di Han ; Li-Li Ye ; Zin Lin; Vassilios Kovanis ; Ying-Cheng Lai

APL Mach. Learn. 2, 036105 (2024)
https://doi.org/10.1063/5.0216271

Deep-learning design of electronic metasurfaces in graphene for quantum control and Dirac electron holography

Cite as: APL Mach. Learn. 2, 036105 (2024); doi: 10.1063/5.0216271
Submitted: 28 April 2024 • Accepted: 23 July 2024 •
Published Online: 9 August 2024

Chen-Di Han,[1] Li-Li Ye,[1] Zin Lin,[2] Vassilios Kovanis,[2,3] and Ying-Cheng Lai[1,4,a)]

AFFILIATIONS

[1] School of Electrical, Computer and Energy Engineering, Arizona State University, Tempe, Arizona 85287, USA
[2] Bradley Department of Electrical and Computer Engineering, Virginia Tech Research Center, 900 N. Glebe Rd., Arlington, Virginia 22203, USA
[3] Virginia Tech National Security Institute, Research Center, 900 North Glebe Rd., Arlington, Virginia 22203, USA
[4] Department of Physics, Arizona State University, Tempe, Arizona 85287, USA

[a)] **Author to whom correspondence should be addressed:** Ying-Cheng.Lai@asu.edu

ABSTRACT

Metasurfaces are sub-wavelength patterned layers for controlling waves in physical systems. In optics, metasurfaces are created by materials with different dielectric constants and are capable of unconventional functionalities. We develop a deep-learning framework for Dirac-material metasurface design for controlling electronic waves. The metasurface is a configuration of circular graphene quantum dots, each created by an electric potential. Employing deep convolutional neural networks, we show that the original scattering wave can be reconstructed with fidelity over 95%, suggesting the feasibility of Dirac electron holography. Additional applications such as plane wave generation and designing broadband and multi-functionality electronic metasurface in graphene are illustrated.

I. INTRODUCTION

Metasurfaces are two-dimensional (2D) arrays of sub-wavelength scatterers. A common form of metasurfaces is metallic or dielectric structures for modulating or controlling electromagnetic waves to achieve desired wavefront, polarization distribution, intensity distribution, or spectrum.[1–6] Optical metasurfaces have wide applications such as planar lens and axicons,[7,8] vortex generators,[9] beam deflectors,[10] and holography.[11,12] Compared with transform optics that requires continuous changes in the refractive index,[13] metasurfaces contain distinct elements and are experimentally feasible. Metasurface design is important for problems such as surface plasmon polarization control and phase and amplitude reconstruction,[14,15] and metasurfaces have been exploited for acoustic[16,17] and water surface wave[18,19] devices as well. Metasurfaces can also be extended to matter waves. For example, in electron holography, information about the electron wave can be stored and reconstructed,[20,21] and the reconstructed wave can provide significantly improved resolution.[22,23]

Optical metasurfaces were invented to manipulate the wavefront and create holography. Naturally, the concept can be extended to other wave systems, such as the low-energy excitations in graphene governed by the Dirac equation. Existing studies of graphene metasurface focused mostly on its optical properties, i.e., its use as a dielectric medium to modulate electromagnetic waves. From the perspective of controlling electronic waves, a previous theoretical study[95] realized different degrees of electron beam bending and splitting using Dirac electronic metasurfaces in graphene under ambient conditions. The electronic graphene metasurfaces thus represent a class of optics-inspired electronic devices that can operate under experimental conditions. However, whether electronic metasurfaces in graphene can be used to create Dirac electron holography remained an open question.

An active area of research is to design metasurfaces according to specific goals.[24] A previous method was based on impedance retrieval that utilizes the local periodicity without optimization,[25,26] requiring large metasurfaces that overlap with the target region. A recent trend is to exploit machine learning,[27,28] where a rigorous

solver of the metasurface scattering physics is approximated and replaced by a back-propagation type of neural network for high computational efficiency (e.g., thousand times faster than traditional optimization method).[29] Another advantage of machine-learning design lies in its tolerance to constraints, in contrast to traditional optimization that relies on explicit but often unavailable constraints. For example, for designing devices with parameters in a fixed region by the interior-point method,[29] generative adversarial neural networks (GANs)[30] or physics-enhanced machine learning[31,32] can be effective. For discrete target space, reinforcement learning can be used for optical metasurface design.[33] Quite recently, physics-informed neural networks for quantum control have been articulated.[34]

In this paper, we address metasurface design for electronic waves in graphene, a widely studied 2D Dirac material.[35–42] Under the continuum approximation, graphene is effectively a thin conducting layer,[43–45] and an electronic metasurface in graphene can be used to manipulate electromagnetic waves,[46–48] with gate potentials generating material layers of different refractive indices,[49–51] thereby offering more flexibility than optical metasurfaces whose properties are fixed once designed. Experimentally, the required gate-potential profiles can be created by STM tip[52–55] or doping.[56] For example, a periodic scattering structure leading to a graphene superlattice was realized,[57–60] with an experimentally observed band structure.[61] A configuration of graphene scatterers can generate complex scattering phenomena,[62] and there were experiments on multiple graphene quantum dots formed by a proper electric potential.[63,64]

We focus on designing an electronic metasurface in graphene to control and manipulate Dirac electron scattering to generate any desired wavefront. Consider a point source emitting Dirac electronic waves with different energies through scattering from an electronic metasurface in graphene. For convenience, the region of observation, or the target region, is a rectangle whose side is approximately twice the wavelength. To be concrete, we assume that the metasurface consists of a small number of, for example, six circular scatterers (quantum dots) of a fixed radius. In the language of Dirac electron optics, the design goal is to find the value of the dielectric constant of each quantum dot to generate any desired electronic waveform in the rectangular region of observation. This is an inverse-design problem of finding the optimal combination of the gate potentials applied to the quantum dots on the metasurface. Because of the need to test a large (infinite in principle) number of parameter combinations, optimization based on a rigorous Dirac equation solver is computationally infeasible. Moreover, estimating the derivatives of the solutions for optimization is challenging due to the need for calculating the inverse matrix at each time step. Our solution is to exploit deep convolutional neural networks (DCNNs) as a simulator for solving the Dirac equation.[65–67] We demonstrate that a designed metasurface of as few as six quantum dots can generate rich types of scattering wave. A phenomenon is that, given an actual scatterer with a complicated geometry, e.g., a star-like scatterer, a DCNN-designed metasurface can generate essentially the identical waveform in the target region, realizing Dirac electron holography. As will be demonstrated, given an optimization goal, it is even possible to generate broadband holography and multi-functional devices. Compared with optical metasurfaces whose physical parameters are fixed at the creation of the device, graphene based metasurfaces have the advantage of flexibility in that the physical parameters can be readily modified through the external gate potentials.

II. ELECTRONIC METASURFACE IN GRAPHENE AND MACHINE-LEARNING DESIGN

A. Scattering physics from an electronic metasurface in graphene

We consider a representative electronic metasurface in graphene consisting of six circular scatterers, as shown in Fig. 1(a). In the single-electron framework, the Hamiltonian is

$$H = v_g \boldsymbol{\sigma} \cdot \mathbf{p} + \sum_{i=1}^{6} V_i(\mathbf{r}), \tag{1}$$

where v_g is the Fermi velocity, $\boldsymbol{\sigma}$ is the vector of Pauli matrices, $\mathbf{p}$ is the momentum of the electron, and $V_i(\mathbf{r})$ is the potential energy profile that defines the ith scatterer, for $i = 1, \ldots, 6$. A typical quantum dot[68] in the configuration in Fig. 1(a) has the radius $r = 0.35\lambda \sim 3.5$ nm with the typical wavelength $\lambda \sim 10$ nm, where the center of each circle is located in the 2D physical domain defined by $x \in \{1, 2\}\lambda$ and $y \in \{-1, 0, 1\}\lambda$. The energy of each potential $V_i(\mathbf{r})$

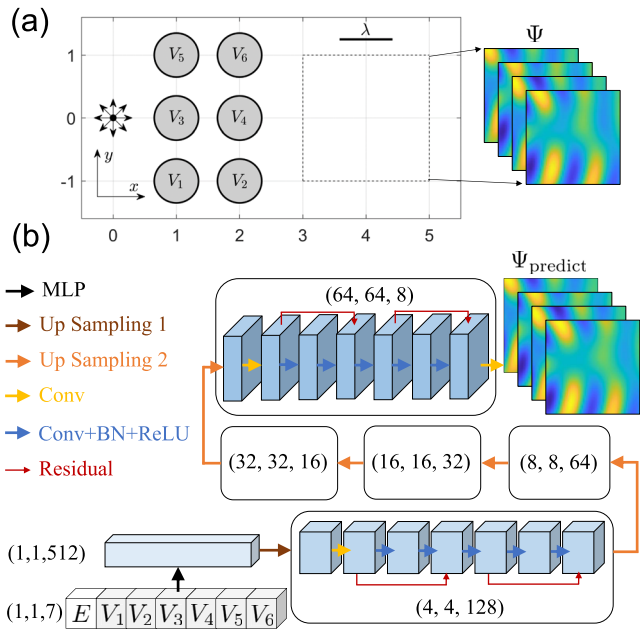

FIG. 1. Structure of the electronic graphene metasurface for quantum scattering and machine-learning design. (a) An electronic metasurface in graphene consisting of six scatterers labeled as V_1 to V_6 in the 2D physical space, where a cylindrical wave of energy E propagates from the left. The square target region on the right is indicated as the dashed box. The output spinor wave function contains two complex components. The four images shown are the real and imaginary parts of the two components in the order: $\Psi = [\mathrm{Re}\,\psi_1, \mathrm{Im}\,\psi_1, \mathrm{Re}\,\psi_2, \mathrm{Im}\,\psi_2]$. (b) A U-net type of convolutional neural network architecture employed in our study, where different arrows indicate interlayer transforms. The six potential values of scatterers and incident energy are served as the 1D input to the neural network. Each rounded rectangle represents one convolutional block of certain size. Up-samplings connect different blocks. The output images contain four channels with the same dimension as that of the spinor wave function.

has the physical unit of $\hbar v_g/\lambda \sim 0.1$ eV, which is created by applying a proper external gate potential in the range from −0.5 to 2 eV. In graphene, the low-energy effective model is obtained by the Taylor expansion about one of the two nonequivalent Dirac points $\xi\mathbf{K} = (\xi 4\pi/(3\sqrt{3}a), 0) \sim (\xi/a, 0)$ with $\xi = \pm 1$ in the hexagonal Brillouin zone. The lattice constant in graphene is $a = 2.46$ Å ~ 0.1 nm. The typical wave vector can be written as $\mathbf{k} = \xi\mathbf{K} + \delta\mathbf{k}$. For $k_y = \delta k_y \sim 0$, we have

$$k_x \sim \xi 4\pi/(3\sqrt{3}a) + \delta k_x \sim \xi/a + 2\pi/\lambda.$$

The typical wavelength in our metasurface system is $\lambda \sim 10$ nm, which is much greater than $a \sim 0.1$ nm, rendering valid the use of the first-order Taylor expansion to obtain the linear dispersion relation for the Dirac fermions. For convenience, we use dimensionless physical quantities. As a result, the geometric structure and the physical properties of metasurfaces for graphene Dirac electrons are readily experimentally controllable, in contrast to optical metasurfaces defined by the material properties such as dielectric constants that cannot be changed once chosen.

For electron holography in three dimensions (3D), energy conservation stipulates that the amplitude of a planar incidence wave decays inversely with the distance to the origin.[69] For a 2D graphene metasurface, the wave function can be written as a two-component spinor $\psi = [\psi_1, \psi_2]^T$, where both components ψ_1 and ψ_2 are complex. The same energy consideration requires that the wave decays with the distance r to the source as $1/\sqrt{r}$. A typical incident spinor wave can then be chosen as

$$\psi_{\text{in}} = \frac{1}{\sqrt{2}} \begin{pmatrix} H_0^{(1)}(\mathbf{r}) \\ iH_1^{(1)}(\mathbf{r})e^{i\theta} \end{pmatrix}, \tag{2}$$

where $H^{(1)}(\mathbf{r})$ is the Hankel function of the first kind. We choose the post-scattering target region to be a square, as shown by the dashed box defined as $x \in [3, 5]$ and $y \in [-1, 1]$ in Fig. 1(a). For machine learning and loss-function computation, real quantities are required, so we introduce the following equivalent real spinor wave function: $\Psi = [\text{Re}\,\psi_1, \text{Im}\,\psi_1, \text{Re}\,\psi_2, \text{Im}\,\psi_2]^T$.

To solve the scattering problem, we use the multiple multipole (MMP) method originated from optics[70–74] and adopted to photonic crystal waveguides[75] and surface plasmons in metallic nanostructures.[73] The method has recently been extended to Dirac–Weyl spinor systems under different geometrical and mass settings.[76–79] For a fixed set of gate potentials and incident energy, the resulting normalized scattering wave in the target region can be calculated using the MMP method, generating a forward solution.

In the multiple multipole method, the wave function is expanded over the pole index $m \in \{0, 1, \ldots, m_{\max}\}$, with $m_{\max}$ being the number of fictitious poles placed around the boundary of the scatterer. For each value of m, the orbital angular momentum index l takes on the value[76] $\{-1, 0, 1\}$. We used this range for the orbital angular momentum index and determined the resulting number $m_{\max}$ of multipoles to satisfy the numerical accuracy for the boundary conditions. The order of the multipole expansion indeed depends on the relative size r of the scatterer compared to the electronic wavelength λ. Intuitively, this selection of the order can be understood by considering two cases. For $r \ll \lambda$, there is no significant scattering, so the expansion order can be low. In contrast, for $r \approx \lambda$ or $r > \lambda$, there is significant scattering. In this case, more poles should be placed in the vicinity of the scatterer boundary.

Our inverse design addresses the problem of identifying an optimal combination of the electrical potentials applied to the scatterers to achieve a desired scattering wave, denoted as Ψ_{target}. Our goal is to solve the following optimization problem:

$$\min_{\mathbf{V}} \|\Psi(\mathbf{V}) - \Psi_{\text{target}}\|^2, \tag{3}$$

where $\mathbf{V}$ denotes the set of gate potentials and $\Psi(\mathbf{V})$ is a forward solution. Obtaining an optimal solution of $\mathbf{V}$ requires repeated use of the MMP method, one use for each potential configuration with variations determined by a gradient, which is computationally costly. Another difficulty lies in finding the gradient, which requires matrix inverse associated with the MMP method, which can be computationally extremely challenging. These difficulties motivated us to exploit machine learning by using convolutional neural networks to approximate $\Psi(\mathbf{V})$.

In optical metasurface design, two different types of problems often arise. One type concerns creating a metasurface to transfer energy, such as a planar lens[7,8] or a beam deflector.[10] For this type of problems, the relevant physical quantity is the absolute light intensity or strength. The second type is holography,[12] which requires reconstructing the phase and amplitude of the wave in some target region. For holography, the relative light strength is relevant since not all the input light energy can be used to construct a holographic object. In this case, the scattering wave inside the target region can be normalized to generate data of suitable scale for machine-learning design.

B. Deep convolutional neural networks

The basic idea of machine-learning design of electronic metasurfaces in graphene is to use a DCNN to substitute the Dirac equation solver (MMP). The input to the DCNN is the structure of the metasurface characterized by a vector of the gate potentials. The output of the DCNN is the spatial distribution of the spinor wave function. Since the wave functions spatially adjacent to each other are correlated as governed by the Dirac equation, DCNN trained to capture such correlations can be used to execute the same function as the Dirac equation. Such a neural network is equivalent to the inverse version of the neural networks typically used in image classification.[80] In particular, for image classification, a decrease in the spatial size is accompanied by a simultaneous increase in the channel size. For our inverse problem, increasing the spatial size then requires decreasing the channel size (to be explained below). In general, using the residual connection and batch normalization (BN) can improve the performance of deep neural networks and reduce overfitting.[66,81]

Figure 1(b) shows the DCNN structure used in our study. The original input is a vector of seven components, one for energy and six for the six gate potential profiles. Since the neural networks require a three-dimensional vector as the input, we add two dummy dimensions, so the input is a three-dimensional matrix: (1,1,7), where the first two dimensions represent the space and the third value denotes the number of channels. After a multilayer perceptron (MLP), the input matrix maps to a 3D matrix of dimension (1,1,512). Up-sampling with convolutional kernel size 4 × 4, stride

TABLE I. Parameters of convolutional layers.

Layer name	Kernel size	Padding	Stride
Up-sampling 1	4 × 4	0	1
Up-sampling 2	4 × 4	0	2
Conv	3 × 3	1	1

1, and zero padding is performed next, where the number of channels is reduced in each up-sampling with a simultaneous increase in the spatial dimension. The next is a convolutional block containing several convolutional layers 3 × 3, stride 1, and 1 padding. It also contains residual connections and batch normalization (BN).[81] After the first block, another up-sampling is performed with convolutional kernel size 4 × 4, stride 2, and 0 padding, converting the 3D matrix into one of dimension (8, 8,64). A similar structure is repeated three times. Finally, when the convolutional block of spatial dimension 64 is done, we use a 2D convolutional layer and set the output dimension to be (64, 64,4). Table I summarizes the three different convolutional layers used in our study. It is worth noting that, even with the same convolutional layer, the number of channels can be different for different blocks.

It is worth comparing our DCNN architecture with two typical neural networks for the inverse design. First, compared with the traditional generative adversarial neural network (GAN) that has recently been adopted for the inverse design,[30] our DCNN architecture contains a residual connection specifically for complicated training data, e.g., output wave function patterns from different energy values. Second, we note that the U-Net originally introduced for the inverse design of medical images does not contain shortcut connections.[65]

The training data are generated as follows: We first set (quite arbitrarily) the energy range to be $E \in [5, 10]$ and choose the gate potential such that $V_i \in [-5, 20]$ (these input data to the neural networks are normalized to the unit interval). As shown in Fig. 1(a), the size of the square target region to observe the scattering patterns of incident cylindrical waves is approximately two or three times of the incident wavelength. We then use the MMP method to calculate the scattering wave functions (see Appendix A for details). The target region is discretized into a 64 × 64 grid, and the wave function at each grid point is obtained. Finally, we normalize the wave function in the target region to generate the training data $\Psi = [\mathrm{Re}\,\psi_1, \mathrm{Im}\,\psi_1, \mathrm{Re}\,\psi_2, \mathrm{Im}\,\psi_2]$. Altogether, we generate 80 000 training datasets (scattering patterns) from randomly generated energy and potential values in their respective ranges. For comparison, with brute-force sampling, since the input data are a seven-dimensional vector, 80 000 training datasets are equivalent to taking only five points in each dimension.

Table II lists the values of the training parameters. The loss function is the mean square error (MSE),

$$\mathcal{L}_{\mathrm{Train}} = \|\Psi_{\mathrm{real}} - \Psi_{\mathrm{predict}}\|^2. \tag{4}$$

The neural network is built using PyTorch,[82] and a graphics processing unit (GPU) is employed for fast training. Figure 2(a) shows the training and validating errors vs the epoch number. The fluctuations

TABLE II. Values of the training parameters for DCNN.

Description	Values
Batch size	128
Learning rate	0.005
Optimizer	Adam
Number of epochs	1000
Number of training data	80 000
Number of validating data	10 000
Number of testing data	10 000

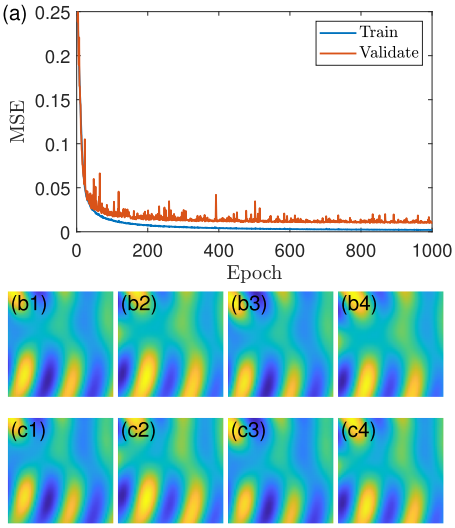

FIG. 2. Performance of DCNN training. (a) Training and validation errors vs epoch number. The errors converge to small values after about 1000 epochs. (b1)–(b4) The true wave function calculated by the MMP method, where the four images from the left to right correspond to the real spinor components Re ψ_1, Im ψ_1, Re ψ_2, and Im ψ_2. (c1)–(c4) The corresponding DCNN predicted spinor components, where the MSE is less than 0.01, similar to the averaging testing error.

are mainly due to batch normalization used in the neural network, which can be reduced by using a larger batch size. However, a large batch slows down the convergence, so there is a computational trade-off. Figures 2(b1)–2(b4) and 2(c1)–2(c4) show the true (calculated from the MMP method) and DCNN predicted scattering wave function from one example in the testing dataset whose MSE is about the average testing error, where the four panels in each row correspond to the four real spinor components Re ψ_1, Im ψ_1, Re ψ_2, and Im ψ_2, respectively. Visually, there is little difference between the DCNN predicted scattering patterns and the ground truth, indicating that effective training has been achieved. Table III lists the MSEs for training, evaluating, and testing from the dataset with the smallest validation error. It can be seen that the training MSE is smaller than the validation and testing MSEs, indicating a certain degree of overfitting. Using more training data can help mitigate this problem.

TABLE III. MSEs from the trained DCNN.

Description	Values
Training MSE	0.0020
Validating MSE	0.0101
Testing MSE	0.0102

III. DIRAC ELECTRON HOLOGRAPHY

A well-trained DCNN can substitute the real Dirac equation solver and provide an accurate solution in a computationally efficient way. In particular, with the available open source packages such as PyTorch,[82] computing the loss and the gradient with respect to the input on GPU servers can be done extremely efficiently. For inverse design, the loss function is

$$\mathcal{L}_{\text{design}} = \|\Psi_{\text{predict}}(\mathbf{V}) - \Psi_{\text{target}}\|^2, \tag{5}$$

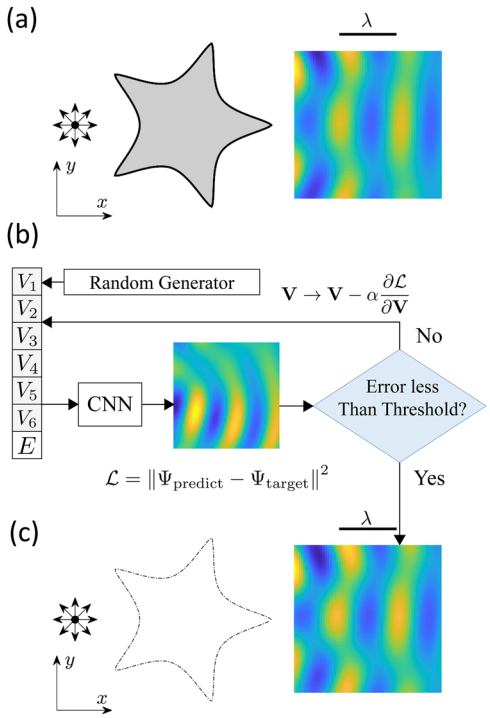

FIG. 3. Inverse design for Dirac electron holography. (a) A real scatterer of a star shape with potential $V = 20$ (details in Appendix B). The scattering wave function in the rectangle region is calculated directly from the star-shaped potential by using the MMP method. Shown on the right is a real component of the scattering wave Re ψ_1. (b) Illustration of the inverse design process. The target wave and the energy are the inputs to the DCNN. Initially, the potential configuration **V** is generated randomly. The DCNN generates the scattering wave and compare it with the target wave in (a), and the error is used to modify the potential configuration **V**. The process is iterated until the loss function is below a pre-selected error threshold, leading to the optimal potential configuration. (c) Scattering wave pattern calculated from the optimal potential configuration through, again, the MMP method, which matches the desired wave pattern in (a), thereby creating a holographic image of the star-shaped scatterer and realizing Dirac electron holography.

where Ψ_{predict} is the output from the neural network and Ψ_{target} is the desired target wave. Figure 3 presents an example of generating a desired wave pattern, optimization, and creating Dirac electron holography. In particular, Fig. 3(a) shows a real scatterer of a star shape generated by the gate potential $V = 20$. For the cylindrical incident wave of energy $E = 8$, the scattering-wave pattern in the target region, calculated directly from this star scatterer using the MMP method (details in Appendix B), is also shown. Figure 3(b) shows the optimization algorithm to minimize the loss in Eq. (5), which starts from a randomly generated potential. We input the initial potential to the neural network and compute the loss and the gradient to variations in the metasurface parameter vector **V** and update **V** by the optimization algorithm (source package scipy.optimize.minimize[83] in Python) at certain learning rate α that depends on the specific optimization method. Note that, since the electron energy as an input to the neural network is given for the design process, we use the potentials to evaluate the gradient. In fact, with the known target wave pattern, the energy can be obtained from the Dirac equation. The optimization result depends on the initial condition, so we use a small ensemble of (ten) initial conditions and choose the potential configuration **V** that yields the smallest value of $\mathcal{L}_{\text{design}}$. This combination of the potential values also gives the smallest loss in Eq. (3) for a properly trained DCNN. To demonstrate that the so-designed metasurface with the optimal potential configuration can generate the desired target wave pattern, we again employ the MMP method to calculate the scattering wave in the target region, but this time from the potential configuration. The resulting scattering wave pattern in shown in Fig. 3(c), which agrees well with that calculated from the star scatterer itself in Fig. 3(a). The DCNN generated metasurface can thus faithfully generate the desired scattering wave pattern from a geometrically complicated scatterer such as a star. Conversely, the metasurface generated wave pattern corresponds to the specific star scatterer, as shown by the dotted-dashed shape in Fig. 3(c), realizing Dirac electron holography!

To characterize the design accuracy, we define the following fidelity measure:

$$F = |\psi_{\text{design}}\psi^*_{\text{target}}|, \tag{6}$$

where ψ_{design} is the normalized scattering wave generated by the metasurface and ψ_{target} is the normalized wave from a target scatterer as governed by the Dirac equation, for the same energy E. In the ideal case where the metasurface generates a wave that matches perfectly the target wave, we have $F = 1$ (due to normalization).

The general principle of holography is scattering wave matching, as can be seen by comparing the desired wave generated by a star-shaped scatterer in Fig. 3(a) and that generated by the designed metasurface in Fig. 3(c). Two more examples are shown in the upper and middle rows in Fig. 4, where the holographic objects have the shape of a circle and a stadium, respectively (the geometric parameters specified in Appendix B). The energy values for the two cases are $E = 8$. For comparison, we also include the case of the star-shaped holographic object (shown in Fig. 3) in the bottom row of Fig. 4. For the three cases, the desired wave patterns are shown in the left column and those generated by the DCNN-designed metasurface are shown in the middle column, with the potential configuration of the metasurface in the right column. It can be seen

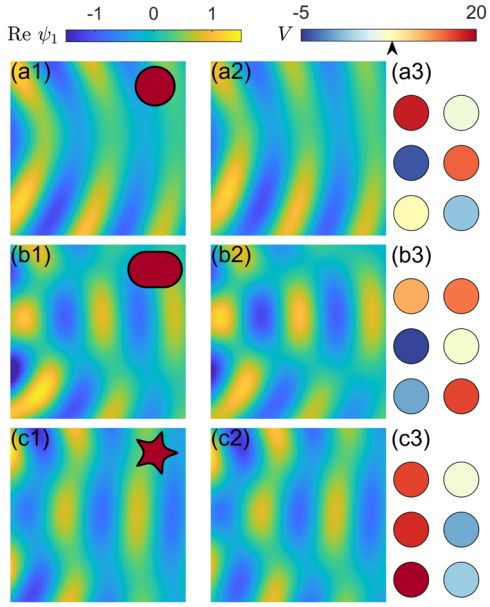

FIG. 4. Examples of scattering-wave matching and Dirac electron holography for three different objects. (a1) Scattering wave from a circular cavity of potential $V = 20$ with cylindrical incident wave of energy $E = 8$, (a2) scattering wave from the DCNN designed metasurface, and (a3) color-coded potential configuration of the designed metasurface. (b1)–(b3) Same legends as in (a1)–(a3) but for a stadium-shaped holographic object. (c1)–(c3) Same legends as in (a1)–(a3) but for a star-shaped holographic object.

that for the three holographic objects, an excellent scattering-wave matching has been achieved. The resulting fidelity values for three different energy values are listed in Table IV. In all cases, the fidelity values are larger than 95%. Note that for a larger energy, the fidelity value decreases slightly due to the target region's containing more wavelengths.

There are some constraints for the loss function Eq. (5), which leads to a metasurface with specific phase matching. A constant phase shift ϕ will not only modify the spinors to $\psi \exp(i\phi)$, but also change the value of the loss function. While phase is important for interference-related problems in quantum system,[84,85] it is not crucial for physical quantities such as the local electron density, current, and pseudospin polarization. For those phase-independent quantities, the loss function Eq. (5) may not yield the best structure. The second constraint is that the absolute information for the amplitude is missing in Eq. (5) due to normalization.

TABLE IV. Fidelity values for a circular, stadium, and star holographic object for different incident energies.

Geometric shape	$E = 7$	$E = 8$	$E = 9$
Circle	0.992	0.965	0.963
Stadium	0.967	0.966	0.961
Star	0.988	0.974	0.959

It is worth noting that, in optical holography, the energy E corresponds to the input frequency and the potential configuration $\mathbf{V}$ represents the dielectric property of the metasurface. If the output is a scattering cross section or transmission, MLPs are commonly used with the output being a vector covering all the frequencies.[29] For graphene metasurface, the aim of our inverse design is to achieve wave function matching, so the DCNN output is a 2×2 matrix representing the scattering wave function. Another difference from the optical metasurface is that the electron energy value E is also input to the neural network, so the output is the wave function but at the specific energy value, enabling faster inverse design.

IV. OTHER APPLICATIONS OF MACHINE-LEARNING DESIGNED ELECTRONIC METASURFACES IN GRAPHENE

We address three additional applications of electronic metasurfaces in graphene.

A. Plane wave generation

An important application of metasurfaces in optical system is to transform a cylindrical wave into another type of wave.[25,26] To demonstrate that this is also possible with our machine-learning based Dirac electron holography, we begin with a spinor plane wave—a simple solution of the Dirac equation,

$$\psi_{\text{plane}} = \begin{pmatrix} 1 \\ \tau \end{pmatrix} \exp(ikx), \tag{7}$$

where $\tau = \text{sign}(E)$ and $k = |E|/v_g$. We normalize the wave and set it as the desired wave pattern in the target region and aim to transform an incident cylindrical wave into this plane wave. Note that, even without metasurface scattering, the cylindrical and plane waves share a certain degree of similarity, especially in the small energy regime, as indicated in the middle column of Table V, where the values of "natural" (i.e., without any scatterer) fidelity between the two types of waves for several energies are listed. It can be seen that the fidelity value is high for small energy and decreases as the energy increases. For a metasurface to be meaningful, for any energy, the achieved fidelity value should be larger than the "natural" value.

Figure 5(a1) shows the spatial pattern of $\text{Re}\{\psi_1\}$ taken from the plane wave for $E = 6$, where the upper-right inset is the incident wave. Figure 5(a2) shows the scattering wave from our DCNN-generated metasurface whose structure is displayed in Fig. 5(a3), where the color for each quantum dot indicates the potential value (red for high positive and blue for low negative values). The black

TABLE V. Fidelity values for the metasurface based graphene plane wave generator.

Energy	Fidelity (natural)	Fidelity (designed)
5	0.972	0.988
6	0.964	0.996
7	0.954	0.989
8	0.942	0.973
9	0.930	0.963
10	0.915	0.966

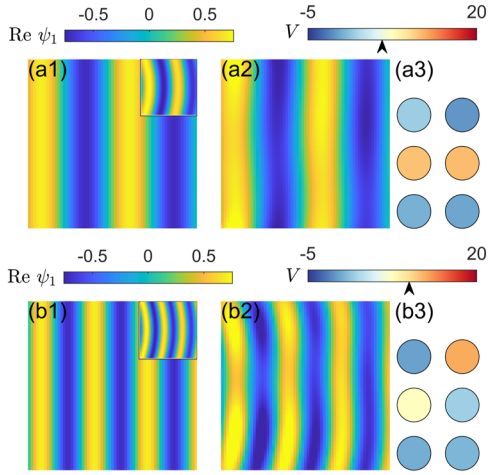

FIG. 5. Illustration of an electronic metasurface plane wave generator. (a1) A desired plane wave in the target region for $E = 6$, where the color represents the strength of $\mathrm{Re}\{\psi_1\}$ and the inset in the top right corner displays the incident cylindrical wave at the same energy. (a2) The plane wave generated by the DCNN designed metasurface for $E = 6$ with the high fidelity value 0.996. (a3) The resulting metasurface of six graphene quantum dots with the color representing the potential strength. The black arrow indicates the energy value. (b1)–(b3) Another example: generating a desired plane wave for $E = 10$. Legends are the same as in (a1)–(a3). The fidelity value is 0.966, which decreases slightly from the value in (a2), due to the higher energy.

arrow pointing at the upper color bar specifies the value of the incident energy. The fidelity achieved in this case is 0.996. The striking similarity between the wave patterns in Figs. 5(a1) and 5(a2) is indicative of the success of the DCNN metasurface design. Another example is shown in Figs. 5(b1)–(b3), for a higher energy value: $E = 10$. The scattering wave pattern from the designed metasurface exhibits oscillations, due to the high energy. The third column of Table V lists the fidelity values from the metasurface generated plane waves for a number of energy values. As the energy increases, there is a slow decrease in the fidelity value. This can be explained by noting that, since the incident cylindrical wave is from the left, the scattering wave amplitude can take larger values on the left than on the right side of the metasurface scatterer, but an ideal plane wave has the same amplitude at any point in the propagation direction [the difference can be seen from Figs. 5(b1) and 5(b2)]. In addition, as the energy increases, the wavelength decreases so that the same target region of observation contains more wavelengths, making it more difficult for the designed metasurface to generate a plane wave in this region.

B. Designing broadband electronic metasurface in graphene

For a metasurface system designed to modulate or control waves, whether optical or Dirac electron waves, bandwidth is an important characterizing quantity. In particular, will the system function as desired in a broad frequency (energy) range or will it work only for specific frequencies (energies)? The bandwidth issue is also crucial in other situations such as designing a wave system for cloaking or superscattering in a certain frequency (energy) range.[67,86,87] As illustrated in Fig. 3, the geometric shape of our DCNN-designed metasurface differs drastically from the actual scatterer. Since the potential configuration defining a specific metasurface was generated through scattering data at certain energies, acceptable wave matching (holography) cannot be anticipated to arise for all energies. Would it be possible to design a metasurface device with the desired functionality in a limited energy range? To address this question, we define the following quantity to characterize the bandwidth:

$$\Delta \equiv (\lambda_{\max} - \lambda_{\min})/\lambda_{\min}, \tag{8}$$

where $\lambda_{\min}$ and $\lambda_{\max}$ are the minimum and maximum wavelengths and the performance of the metasurface system is acceptable for any wavelength $\lambda \in [\lambda_{\min}, \lambda_{\max}]$. A similar quantity was introduced, for example, in a previous study on designing a strong scattering system,[29] where a suitable set of loss functions leading to strong scattering was effective even with about a 25% shift in the wavelength. In another work,[88] the geometrical phase was exploited to tolerate a 100% wavelength shift in the inverse design.

Our goal is to assess whether Dirac electron holography can be designed to function in a relatively broad energy range. To gain insights, we consider a circular graphene scatterer. Figure 6(a) shows the scattering wave pattern as a solution of the Dirac equation in the observational region for $E = 7.5$, where the scatterer is generated by the gate potential $V = 20$. Figure 6(b) shows the wave pattern from the corresponding metasurface at the same energy, which matches the actual pattern to a large extent. The question is if the energy is changed, can a reasonable match between the two scattering wave patterns hold? To answer this question, we calculate the fidelity characterizing the wave-pattern matching for a wide energy range, as shown in Fig. 6(c), where the metasurface is designed for $E = 7.5$ (indicated by the black solid circle) for which the fidelity value is 0.980. The vertical gray strip indicates the energy interval in which the fidelity is higher than 0.975. As the energy deviates from this interval, the fidelity value decreases rapidly, so the gray interval represents the bandwidth of the specific design, which is quite narrow relatively as it indicates that the design can tolerate only $\Delta = 3\%$ of the wavelength change.

We use the method of interval-training[29] to increase the bandwidth of the designed metasurface. The idea is to use the wave patterns in an energy interval $[E_1, E_2]$ for the inverse design. The corresponding loss function is

$$\mathcal{L}_{\text{design}} = \int_{E_1}^{E_2} \|\Psi_{\text{predict}}(E, \mathbf{V}) - \Psi_{\text{target}}(E)\|^2 dE. \tag{9}$$

If the energy interval $[E_1, E_2]$ is relatively narrow, the loss function can be approximated by

$$\begin{aligned}\mathcal{L}_{\text{design}} =& \|\Psi_{\text{predict}}(E_1, \mathbf{V}) - \Psi_{\text{target}}(E_1)\|^2 \\ &+ \|\Psi_{\text{predict}}(E_2, \mathbf{V}) - \Psi_{\text{target}}(E_2)\|^2.\end{aligned} \tag{10}$$

To test the loss function in Eq. (10), we set $E_1 = 6$ and $E_2 = 7$ and then minimize the loss to find the potential configuration $\mathbf{V}$. The true and metasurface-generated scattering wave patterns for the two energies are shown in Figs. 6(d)–6(g), and Fig. 6(h) shows the fidelity

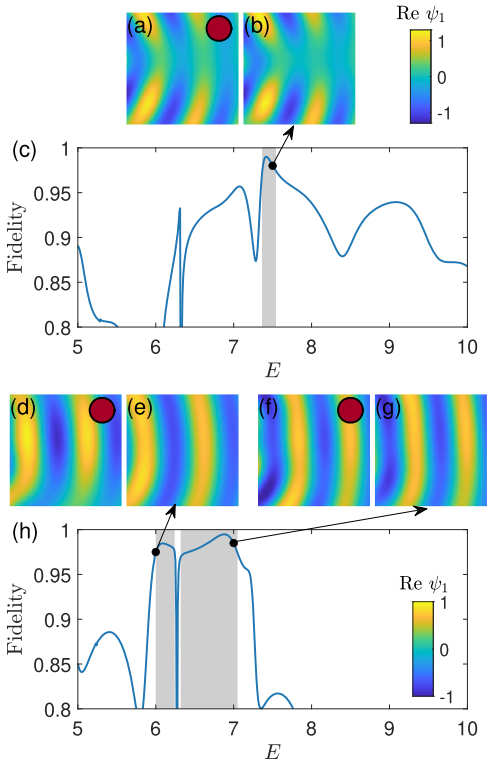

FIG. 6. Wideband metasurface design illustrated using a circular scatterer. The circular scatterer is generated by gate potential $V = 20$. (a) The scattering wave pattern $\mathrm{Re}\{\psi_1\}$ as a solution of the Dirac equation in the target observational region for $E = 7.5$. (b) The wave pattern from the metasurface designed for the same energy. (c) The fidelity vs the energy, where the same metasurface (designed for $E = 7.5$) is applied to all energy values. The black dot indicates the energy $E = 7.5$, and the vertical gray strip indicates the energy interval in which the fidelity value is larger than 0.975, which gives the bandwidth $\Delta \approx 3\%$ in terms of wavelength. (d) The actual wave pattern for $E = 6$. (e) The wave pattern generated by the metasurface designed for $E = 6$. (f) The actual wave pattern for $E = 7$. (g) The wave pattern generated by the metasurface designed for $E = 7$. (h) Fidelity vs the incident energy, where the metasurface is designed using two energy values: $E = 6$ and $E = 7$ (indicated by the two black dots). For most energies in between them, the fidelity value is high. The corresponding bandwidth has been increased to $\Delta \approx 17\%$ of the wavelength.

vs the energy for $E \in [5, 10]$, where the two black dots indicate the two energy values required by the loss function Eq. (10). For most energy values in the vertical gray shaded regions (except for a sharp drop about $E = 6.3$), the fidelity value is larger than 0.975, giving the wavelength bandwidth $\Delta \approx 17\%$—a significant improvement compared with that from a single energy loss function, as shown in Fig. 6(c).

C. Designing multi-functionality electronic metasurface in graphene

In optics, designing metasurfaces that can perform multiple functions was investigated.[89] For example, complicated metasurfaces can generate different holographic patterns at different frequencies.[90] Factors that can change the device properties include phase transition[91,92] and biases.[93,94] Here, we address the problem of designing multi-functionality electronic metasurfaces in graphene through some proper gate potential configuration $\mathbf{V}$. To illustrate our approach, we consider two energy values E_1 and E_2, where the desired scattering wave patterns for the two energy values are different. For example, for E_1, the desired wave pattern should match that from a circular quantum dot, while for E_2, the metasurface generated wave pattern should approximate that from a star-shaped quantum dot, as shown in Figs. 7(a)–7(d). The loss function is

$$\mathcal{L}_{\text{design}} = \|\Psi_{\text{predict}}(E_1, \mathbf{V}) - \Psi_{\text{target1}}\|^2 + \|\Psi_{\text{predict}}(E_2, \mathbf{V}) - \Psi_{\text{target2}}\|^2. \tag{11}$$

As a concrete example, we set $E_1 = 6$ and $E_2 = 8.5$ and perform optimization of the loss function to obtain the optimal potential configuration $\mathbf{V}$. Figure 7(e) shows the fidelity vs the energy E, where the blue (orange) trace is the fidelity with respect to the scattering wave from the circular (star-shaped) quantum dot, with the respective shaded strips in which the fidelity value is larger than 0.975. The result suggests that two different functionalities can be realized by the designed electronic metasurface in graphene with two different energy intervals, respectively. Empirically, the two energy values should not be too close to each other. In addition, assigning a higher energy value for a more complicated scattering pattern (e.g., star-shaped dot) can be beneficial for the optimization process. An intuitive reason is that scattering patterns are generally more complicated at high energies, so using a complicated scatterer at a high energy value can provide more complexity to the neural network to

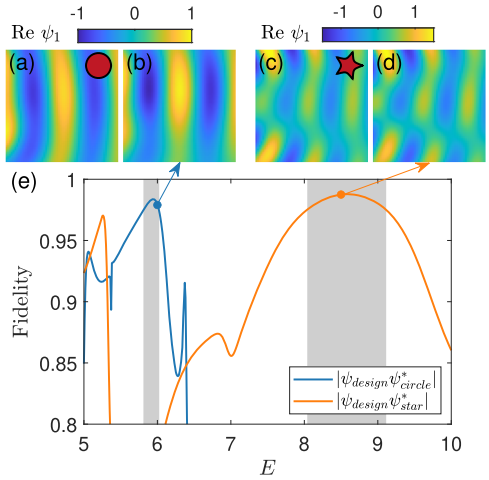

FIG. 7. An example of designing an electronic metasurface in graphene with multiple functionalities. (a) Desired scattering wave from a circular scatterer for $V = 19$ for $E = 6$. (b) The corresponding wave pattern generated by the metasurface for $E = 6$. (c) Desired wave pattern from a star-shaped scatterer for $V = 19$ at $E = 8.5$. (d) The corresponding wave pattern generated by the metasurface for $E = 8.5$. (e) Two types of fidelity vs the energy: blue (orange) trace—fidelity between the desired wave from the circular (star-shaped) quantum dot and the corresponding metasurface-generated wave. The vertical gray shading strips indicate the energy interval with fidelity higher than 0.975. The designed metasurface is capable of double-functional holography in two different energy intervals.

enhance its computational capability and to generate a broad range of solutions of the Dirac equation.

V. DISCUSSION

We have investigated whether electronic metasurfaces in graphene can be exploited to create Dirac electron holography. In particular, we developed a deep-learning based, inverse-design framework to generate "electronic" graphene metasurfaces. The prototypical type of metasurfaces consists of a small number of quantum dots on a graphene sheet, which can be realized through external electric gate voltages. In particular, the voltages applied to the quantum dots are different and constitute a set of parameters that can be optimized through machine learning. As an example, we demonstrated, using an electron graphene metasurface of six quantum dots, that various desired electronic wave patterns can be generated through quantum scattering, thereby realizing Dirac electron holography in graphene.

Our machine-learning design is to train a DCNN trained to generate a relation between a set of device parameters (e.g., the gate voltages) and a desired waveform that can be a plane wave or the scattering wave from a scatterer with a particular geometric shape. Training is done in an "offline" fashion to generate the required parameters for the metasurface. In the case of a single target wave, the wave generated by the metasurface can match the desired wave with fidelity higher than 95%. Such a high-fidelity wave matching is essentially what is required for producing Dirac electron holograph. For metasurfaces generated from training data from a single energy value, waveform matching can be achieved in a small interval about this energy value. To increase the energy (frequency) band, we articulated a loss function that involves the desired and deep-learning predicted wave functions at multiple energy values. Dual functionalities were also demonstrated where a metasurface system can realize Dirac electron holography at two distinct energy values.

One requirement in our framework is that the designed metasurface functions for the same energy values used to generate the waveforms for training. In machine learning, this is referred to as the problem of "overlapping of the design space with the training space." This is in fact a common difficulty for the inverse design of wave scattering systems. Another challenge is that, during the training process, the DCNNs are updated iteratively, which requires a large computational load. Use of generative adversarial neural networks[30] can reduce the computations, as it directly finds a relation between the desired performance and the device parameters. A difficulty is that the device parameters so produced can often be unphysical, requiring some sophisticated filtering process to obtain physical reasonable parameter values.

The importance of many-body effects in graphene was recognized earlier.[96] However, there are situations where the many-body effects can be neglected. Specifically, the physical mechanism rendering graphene a weakly interacting system was investigated, suggesting that the effective fine-structure constant, denoted as $\alpha_{\text{eff}} = e^2/(\hbar v_g \epsilon)$, can be used to gauge the importance of the Coulomb interaction in graphene.[97] For graphene suspended in vacuum, it is theoretically estimated that, for $\alpha_g = 2.2 > 1/137$, the electron–electron interactions are strong and cannot be neglected. For $\alpha_g < 1$, the Coulomb interactions are relatively weak compared to the kinetic energy of the charge carriers, so the many-body effect can be neglected. For a freestanding graphene sheet, experimental studies reported a substantially smaller fine-structure constant:[98] $\alpha_g \approx 0.14$. Another experimental result was that the optical transparency of graphene is consistent with that of non-interacting Dirac Fermions in suspended graphene.[99] Previous studies also demonstrated that graphene nanoribbons with zigzag edges exhibit electronic screening of the long-range Coulomb interaction.[100]

The multiple multipole method was originated from optics, where no equivalence to the many-body effects in electronic systems exists. In fact, this method is a numerical technique for electromagnetic field calculations developed for systems with isotropic, linear, and piecewise homogeneous material properties, and the method is not effective when many-body effects exist.[75] In our work of Dirac electron scattering, the original multipolar functions are replaced by the spinor cylindrical bases. However, including many-body effects such as the Coulomb interaction adds strong nonlinearity to the problem and makes choosing the appropriate basis for multipoles infeasible. To our knowledge, at the present, developing a multiple multipole method for electronic systems incorporating many-body effects is an unsolved problem. It is worth noting that there are traditional methods to calculate the many-body effects in graphene, such as the renormalization-group analysis,[101] mean-field theory,[102] quantum Monte Carlo method,[103] *ab initio* many-body GW method,[104] and many-body Green's function theory.[105]

The ability to control Dirac electron waves through electronic metasurfaces in graphene, as demonstrated in this work, is in the initial exploratory stage. A difficulty associated with generating Dirac electron holography is that, in 2D scattering, the wave amplitude on the front side of the target observational region closer to the source is larger than that on the opposite side. Another feature is that Klein tunneling occurs only at some specific incident angles, so, for vast majority of the incident angles, electron scattering is strong. To our knowledge, prior to our work, Dirac electron holography had not been reported. Our work demonstrates the possibility of manipulating and controlling Dirac waves with the aid of modern machine learning.

ACKNOWLEDGMENTS

This work was supported by the Air Force Office of Scientific Research (AFOSR) under Grant No. FA9550-21-1-0438. V.K. was supported in part by IDQ (a Quantum Communications Company) and by NSF under Grant No. NSF-2328991. This work was also supported by the Office of Naval Research under Grant No. N00014-24-1-2548.

AUTHOR DECLARATIONS

Conflict of Interest

The authors have no conflicts to disclose.

Author Contributions

All designed the research project, the models, and methods. C.-D.H. performed the computations. All analyzed the data. C.-D.H. and Y.-C.L. wrote the paper.

Chen-Di Han: Conceptualization (equal); Formal analysis (lead); Investigation (lead); Methodology (lead); Writing – original draft (supporting); Writing – review & editing (supporting). **Li-Li Ye**: Conceptualization (equal); Investigation (equal). **Zin Lin**: Conceptualization (supporting); Investigation (supporting). **Vassilios Kovanis**: Conceptualization (supporting); Investigation (supporting). **Ying-Cheng Lai**: Conceptualization (equal); Funding acquisition (equal); Project administration (equal); Resources (equal); Supervision (equal); Writing – original draft (equal); Writing – review & editing (equal).

DATA AVAILABILITY

The data that support the findings of this study are openly available in GitHub at https://github.com/hanchendi/Dirac-Electron-Holography.

APPENDIX A: GENERATING DATA USING MULTIPLE MULTIPOLE METHOD

Our training data are the scattering waveforms from a sophisticated scatterer, such as a star-shaped quantum dot, which are generated by the MMP method originated in optics[70–75] and adopted to Dirac–Weyl spinor systems.[76–79] After an electronic metasurface in graphene has been designed, testing it also requires solving the scattering field from it, which is also done using the MMP method. Take the metasurface of six quantum dots as an example. The basic idea of MMP is to place poles both inside and outside of each boundary, as shown in Fig. 8(a). The wave function outside the metasurface is determined by all the poles inside the circular boundaries, and the corresponding poles outside each circular boundary determine the wave function inside the circle. The detailed computational procedure can be found in Ref. 79.

In our calculation, poles inside each circle are located at $r_i = 0.9r$ at the same angular interval. The number of poles inside each circle is $N_i = 40$. Poles outside the circle are located at $r_o = 1.1r$, and their number is $N_o = 44$. The boundary is discretized with $N_j = 3(N_i + N_j)$ points. Each pole generates three values of the angular momentum: $l = \{-1, 0, 1\}$. For a given metasurface, calculating the scattering waveform requires solving roughly 3000 equations with ~1500 unknown parameters. Figure 8(b) shows a typical histogram of the MMP boundary fitting errors,[76] which are sufficiently small to guarantee accurate wave solutions. Altogether, about 10^5 waveforms are produced for the results reported in this paper.

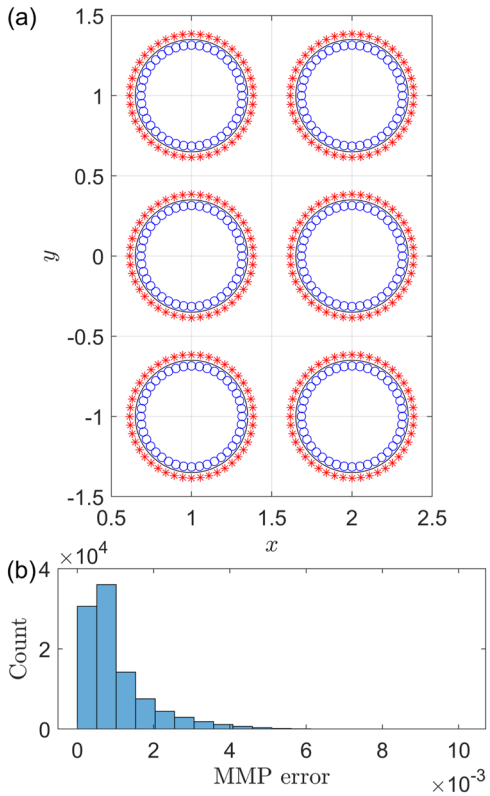

FIG. 8. MMP method for solving the scattering waveform from a graphene metasurface and numerical error. (a) Illustration of the poles inside and outside each circular scatterer. (b) Histogram of the boundary fitting error. In all cases, the values of the energy and potentials are randomly generated.

APPENDIX B: GENERATING TARGET SCATTERING WAVE

The desired target waveforms are calculated using the MMP method for the geometrical structures shown in Figs. 9(a)–9(c). The circle in Fig. 9(a) has the radius $r_c = 1$ and is centered at $[1.5, 0]$. The

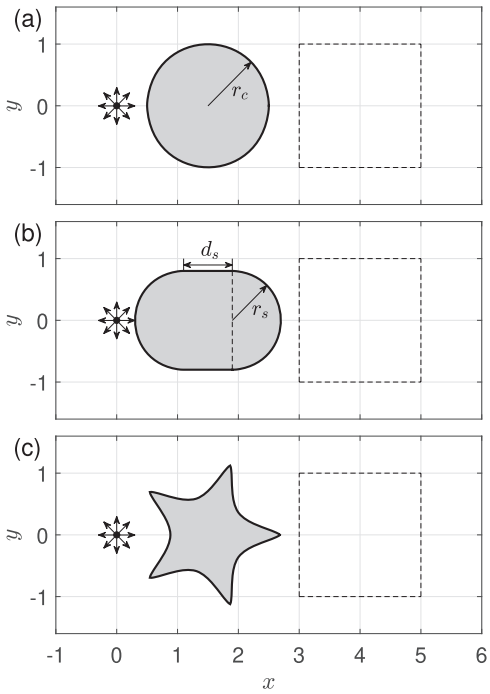

FIG. 9. Different graphene quantum scatterers for generating desired waveforms. (a) A circular quantum dot of radius $r_c = 1$. (b) A stadium quantum dot with parameters $r_s = d_s = 0.8$. (c) A star quantum dot with the boundary determined by the Gielis formula.

two geometric parameters defining the stadium scatterer in Fig. 9(b) are $r_s = d_s = 0.8$, and the center is located at [1.5, 0]. The shape of the star scatterer is determined by the Gielis formula,[106]

$$r(\theta) = \frac{m_3}{\left[\left|\frac{1}{a}\cos\left(\frac{m_1\theta}{4}\right)\right|^{n_1} + \left|\frac{1}{b}\sin\left(\frac{m_2\theta}{4}\right)\right|^{n_2}\right]^{1/n_3}}, \tag{B1}$$

with the parameters $m_1 = m_2 = 10$, $m_3 = 1.2$, $a = 0.98$, $b = 0.28$, $n_1 = 2.33$, $n_2 = 1.46$, and $n_3 = 2.79$. The center of the star is located at [1.5, 0].

REFERENCES

[1] A. V. Kildishev, A. Boltasseva, and V. M. Shalaev, "Planar photonics with metasurfaces," Science **339**, 1232009 (2013).
[2] N. Yu and F. Capasso, "Flat optics with designer metasurfaces," Nat. Mater. **13**, 139–150 (2014).
[3] H.-T. Chen, A. J. Taylor, and N. Yu, "A review of metasurfaces: Physics and applications," Rep. Prog. Phys. **79**, 076401 (2016).
[4] P. Lalanne and P. Chavel, "Metalenses at visible wavelengths: Past, present, perspectives," Laser Photonics Rev. **11**, 1600295 (2017).
[5] S. M. Kamali, E. Arbabi, A. Arbabi, and A. Faraon, "A review of dielectric optical metasurfaces for wavefront control," Nanophotonics **7**, 1041–1068 (2018).
[6] A. M. Shaltout, V. M. Shalaev, and M. L. Brongersma, "Spatiotemporal light control with active metasurfaces," Science **364**, eaat3100 (2019).
[7] F. Aieta, P. Genevet, M. A. Kats, N. Yu, R. Blanchard, Z. Gaburro, and F. Capasso, "Aberration-free ultrathin flat lenses and axicons at telecom wavelengths based on plasmonic metasurfaces," Nano Lett. **12**, 4932–4936 (2012).
[8] X. Ni, S. Ishii, A. V. Kildishev, and V. M. Shalaev, "Ultra-thin, planar, Babinet-inverted plasmonic metalenses," Light: Sci. Appl. **2**, e72 (2013).
[9] P. Genevet, N. Yu, F. Aieta, J. Lin, M. A. Kats, R. Blanchard, M. O. Scully, Z. Gaburro, and F. Capasso, "Ultra-thin plasmonic optical vortex plate based on phase discontinuities," Appl. Phys. Lett. **100**, 013101 (2012).
[10] M. I. Shalaev, J. Sun, A. Tsukernik, A. Pandey, K. Nikolskiy, and N. M. Litchinitser, "High-efficiency all-dielectric metasurfaces for ultracompact beam manipulation in transmission mode," Nano Lett. **15**, 6261–6266 (2015).
[11] X. Ni, A. V. Kildishev, and V. M. Shalaev, "Metasurface holograms for visible light," Nat. Commun. **4**, 2807 (2013).
[12] L. Huang, S. Zhang, and T. Zentgraf, "Metasurface holography: From fundamentals to applications," Nanophotonics **7**, 1169–1190 (2018).
[13] J. B. Pendry, D. Schurig, and D. R. Smith, "Controlling electromagnetic fields," Science **312**, 1780–1782 (2006).
[14] I. Dolev, I. Epstein, and A. Arie, "Surface-plasmon holographic beam shaping," Phys. Rev. Lett. **109**, 203903 (2012).
[15] Q. Xu, X. Zhang, Y. Xu, C. Ouyang, Z. Tian, J. Gu, J. Li, S. Zhang, J. Han, and W. Zhang, "Polarization-controlled surface plasmon holography," Laser Photonics Rev. **11**, 1600212 (2017).
[16] Y. Yang, H. Wang, F. Yu, Z. Xu, and H. Chen, "A metasurface carpet cloak for electromagnetic, acoustic and water waves," Sci. Rep. **6**, 20219 (2016).
[17] B. Assouar, B. Liang, Y. Wu, Y. Li, J.-C. Cheng, and Y. Jing, "Acoustic metasurfaces," Nat. Rev. Mater. **3**, 460–472 (2018).
[18] H. Sun, J. Wang, Y. Cheng, Q. Wei, and X. Liu, "Modulation of water surface waves with a coiling-up-space metasurface," AIP Adv. **6**, 055017 (2016).
[19] S. Zou, Y. Xu, R. Zatianina, C. Li, X. Liang, L. Zhu, Y. Zhang, G. Liu, Q. H. Liu, H. Chen, and Z. Wang, "Broadband waveguide cloak for water waves," Phys. Rev. Lett. **123**, 074501 (2019).
[20] A. Tonomura, "Applications of electron holography," Rev. Mod. Phys. **59**, 639 (1987).
[21] H. Lichte and M. Lehmann, "Electron holography—basics and applications," Rep. Prog. Phys. **71**, 016102 (2007).
[22] A. Tonomura, T. Matsuda, and J. Endo, "High resolution electron holography with field emission electron microscope," Jpn. J. Appl. Phys. **18**, 9 (1979).
[23] A. Orchowski, W. Rau, and H. Lichte, "Electron holography surmounts resolution limit of electron microscopy," Phys. Rev. Lett. **74**, 399 (1995).
[24] M. M. Elsawy, S. Lanteri, R. Duvigneau, J. A. Fan, and P. Genevet, "Numerical optimization methods for metasurfaces," Laser Photonics Rev. **14**, 1900445 (2020).
[25] X. Wan, Y. B. Li, B. G. Cai, and T. J. Cui, "Simultaneous controls of surface waves and propagating waves by metasurfaces," Appl. Phys. Lett. **105**, 121603 (2014).
[26] E. Martini, M. Mencagli, Jr., and S. Maci, "Metasurface transformation for surface wave control," Philos. Trans. R. Soc., A **373**, 20140355 (2015).
[27] S. So, T. Badloe, J. Noh, J. Bravo-Abad, and J. Rho, "Deep learning enabled inverse design in nanophotonics," Nanophotonics **9**, 1041–1057 (2020).
[28] P. R. Wiecha, A. Arbouet, C. Girard, and O. L. Muskens, "Deep learning in nano-photonics: Inverse design and beyond," Photonics Res. **9**, B182–B200 (2021).
[29] J. Peurifoy, Y. Shen, L. Jing, Y. Yang, F. Cano-Renteria, B. G. DeLacy, J. D. Joannopoulos, M. Tegmark, and M. Soljačić, "Nanophotonic particle simulation and inverse design using artificial neural networks," Sci. Adv. **4**, eaar4206 (2018).
[30] Z. Liu, D. Zhu, S. P. Rodrigues, K.-T. Lee, and W. Cai, "Generative model for the inverse design of metasurfaces," Nano Lett. **18**, 6570–6576 (2018).
[31] J. Jiang and J. A. Fan, "Global optimization of dielectric metasurfaces using a physics-driven neural network," Nano Lett. **19**, 5366–5372 (2019).
[32] M. Chen, R. Lupoiu, C. Mao, D.-H. Huang, J. Jiang, P. Lalanne, and J. A. Fan, "High speed simulation and freeform optimization of nanophotonic devices with physics-augmented deep learning," ACS Photonics **9**, 3110–3123 (2022).
[33] I. Sajedian, T. Badloe, and J. Rho, "Optimisation of colour generation from dielectric nanostructures using reinforcement learning," Opt. Express **27**, 5874–5883 (2019).
[34] A. Norambuena, M. Mattheakis, F. J. González, and R. Coto, "Physics-informed neural networks for quantum control," Phys. Rev. Lett. **132**, 010801 (2024).
[35] K. S. Novoselov, A. K. Geim, S. V. Morozov, D.-e. Jiang, Y. Zhang, S. V. Dubonos, I. V. Grigorieva, and A. A. Firsov, "Electric field effect in atomically thin carbon films," Science **306**, 666–669 (2004).
[36] K. S. Novoselov, A. K. Geim, S. V. Morozov, D. Jiang, M. I. Katsnelson, I. Grigorieva, S. Dubonos, and a. Firsov, "Two-dimensional gas of massless Dirac fermions in graphene," Nature **438**, 197–200 (2005).
[37] V. Gusynin and S. Sharapov, "Unconventional integer quantum hall effect in graphene," Phys. Rev. Lett. **95**, 146801 (2005).
[38] A. Rycerz, J. Tworzydło, and C. Beenakker, "Valley filter and valley valve in graphene," Nat. Phys. **3**, 172–175 (2007).
[39] W. Han, R. K. Kawakami, M. Gmitra, and J. Fabian, "Graphene spintronics," Nat. Nanotechnol. **9**, 794–807 (2014).
[40] Y. Cao, V. Fatemi, S. Fang, K. Watanabe, T. Taniguchi, E. Kaxiras, and P. Jarillo-Herrero, "Unconventional superconductivity in magic-angle graphene superlattices," Nature **556**, 43–50 (2018).
[41] Y. Cao, V. Fatemi, A. Demir, S. Fang, S. L. Tomarken, J. Y. Luo, J. D. Sanchez-Yamagishi, K. Watanabe, T. Taniguchi, E. Kaxiras *et al.*, "Correlated insulator behaviour at half-filling in magic-angle graphene superlattices," Nature **556**, 80–84 (2018).
[42] A. H. Castro Neto, F. Guinea, N. M. Peres, K. S. Novoselov, and A. K. Geim, "The electronic properties of graphene," Rev. Mod. Phys. **81**, 109 (2009).
[43] V. Gusynin, S. Sharapov, and J. Carbotte, "Unusual microwave response of Dirac quasiparticles in graphene," Phys. Rev. Lett. **96**, 256802 (2006).
[44] S. A. Mikhailov and K. Ziegler, "New electromagnetic mode in graphene," Phys. Rev. Lett. **99**, 016803 (2007).
[45] L. A. Falkovsky, "Optical properties of graphene," J. Phys.: Conf. Ser. **129**, 012004 (2008).
[46] A. Fallahi and J. Perruisseau-Carrier, "Design of tunable biperiodic graphene metasurfaces," Phys. Rev. B **86**, 195408 (2012).
[47] Z. Miao, Q. Wu, X. Li, Q. He, K. Ding, Z. An, Y. Zhang, and L. Zhou, "Widely tunable terahertz phase modulation with gate-controlled graphene metasurfaces," Phys. Rev. X **5**, 041027 (2015).
[48] T. Guo and C. Argyropoulos, "Broadband polarizers based on graphene metasurfaces," Opt. Lett. **41**, 5592–5595 (2016).
[49] P. E. Allain and J.-N. Fuchs, "Klein tunneling in graphene: Optics with massless electrons," Eur. Phys. J. B **83**, 301–317 (2011).

[50]T. Ozawa, A. Amo, J. Bloch, and I. Carusotto, "Klein tunneling in driven-dissipative photonic graphene," Phys. Rev. A **96**, 013813 (2017).
[51]C.-D. Han, C.-Z. Wang, H.-Y. Xu, D. Huang, and Y.-C. Lai, "Decay of semiclassical massless Dirac fermions from integrable and chaotic cavities," Phys. Rev. B **98**, 104308 (2018).
[52]Y. Zhao, J. Wyrick, F. D. Natterer, J. F. Rodriguez-Nieva, C. Lewandowski, K. Watanabe, T. Taniguchi, L. S. Levitov, N. B. Zhitenev, and J. A. Stroscio, "Creating and probing electron whispering-gallery modes in graphene," Science **348**, 672–675 (2015).
[53]J. Lee, D. Wong, J. Velasco Jr, J. F. Rodriguez-Nieva, S. Kahn, H.-Z. Tsai, T. Taniguchi, K. Watanabe, A. Zettl, F. Wang *et al.*, "Imaging electrostatically confined Dirac fermions in graphene quantum dots," Nat. Phys. **12**, 1032–1036 (2016).
[54]C. Gutiérrez, L. Brown, C.-J. Kim, J. Park, and A. N. Pasupathy, "Klein tunnelling and electron trapping in nanometre-scale graphene quantum dots," Nat. Phys. **12**, 1069–1075 (2016).
[55]F. Ghahari, D. Walkup, C. Gutiérrez, J. F. Rodriguez-Nieva, Y. Zhao, J. Wyrick, F. D. Natterer, W. G. Cullen, K. Watanabe, T. Taniguchi *et al.*, "An on/off berry phase switch in circular graphene resonators," Science **356**, 845–849 (2017).
[56]J. Velasco, Jr., L. Ju, D. Wong, S. Kahn, J. Lee, H.-Z. Tsai, C. Germany, S. Wickenburg, J. Lu, T. Taniguchi *et al.*, "Nanoscale control of rewriteable doping patterns in pristine graphene/boron nitride heterostructures," Nano Lett. **16**, 1620–1625 (2016).
[57]C. Bai and X. Zhang, "Klein paradox and resonant tunneling in a graphene superlattice," Phys. Rev. B **76**, 075430 (2007).
[58]R. P. Tiwari and D. Stroud, "Tunable band gap in graphene with a noncentrosymmetric superlattice potential," Phys. Rev. B **79**, 205435 (2009).
[59]P. Burset, A. L. Yeyati, L. Brey, and H. Fertig, "Transport in superlattices on single-layer graphene," Phys. Rev. B **83**, 195434 (2011).
[60]M. Killi, S. Wu, and A. Paramekanti, "Band structures of bilayer graphene superlattices," Phys. Rev. Lett. **107**, 086801 (2011).
[61]L. Ponomarenko, R. Gorbachev, G. Yu, D. Elias, R. Jalil, A. Patel, A. Mishchenko, A. Mayorov, C. Woods, J. Wallbank *et al.*, "Cloning of Dirac fermions in graphene superlattices," Nature **497**, 594–597 (2013).
[62]M. Sadrara and M. Miri, "Dirac electron scattering from a cluster of electrostatically defined quantum dots in graphene," Phys. Rev. B **99**, 155432 (2019).
[63]Z.-Q. Fu, Y. Pan, J.-J. Zhou, K.-K. Bai, D.-L. Ma, Y. Zhang, J.-B. Qiao, H. Jiang, H. Liu, and L. He, "Relativistic artificial molecules realized by two coupled graphene quantum dots," Nano Lett. **20**, 6738–6743 (2020).
[64]Q. Yang, Y. Zhang, Z.-Q. Fu, Y. Chen, Z. Di, and L. He, "Creating custom-designed patterns of nanoscale graphene quantum dots," 2D Mater. **9**, 021002 (2022).
[65]O. Ronneberger, P. Fischer, and T. Brox, "U-Net: Convolutional networks for biomedical image segmentation," in *Medical Image Computing and Computer-Assisted Intervention – MICCAI* (Springer, 2015), pp. 234–241.
[66]K. He, X. Zhang, S. Ren, and J. Sun, "Deep residual learning for image recognition," in *Proceedings of the IEEE Conference on Computer Vision and Pattern Recognition* (IEEE, 2016), pp. 770–778.
[67]C.-D. Han and Y.-C. Lai, "Generating extreme quantum scattering in graphene with machine learning," Phys. Rev. B **106**, 214307 (2022).
[68]C. B. Murray, C. R. Kagan, and M. G. Bawendi, "Synthesis and characterization of monodisperse nanocrystals and close-packed nanocrystal assemblies," Annu. Rev. Mater. Sci. **30**, 545–610 (2000).
[69]J. Barton, "Removing multiple scattering and twin images from holographic images," Phys. Rev. Lett. **67**, 3106 (1991).
[70]Y. Leviatan and A. Boag, "Analysis of electromagnetic scattering from dielectric cylinders using a multifilament current model," IEEE Trans. Antennas Propag. **35**, 1119–1127 (1987).
[71]M. G. Imhof, "Multiple multipole expansions for elastic scattering," J. Acoust. Soc. Am. **100**, 2969–2979 (1996).
[72]D. I. Kaklamani and H. T. Anastassiu, "Aspects of the method of auxiliary sources (MAS) in computational electromagnetics," IEEE Antennas Propag. Mag. **44**, 48–64 (2002).
[73]E. Moreno, D. Erni, C. Hafner, and R. Vahldieck, "Multiple multipole method with automatic multipole setting applied to the simulation of surface plasmons in metallic nanostructures," J. Opt. Soc. Am. A **19**, 101–111 (2002).
[74]G. Tayeb and S. Enoch, "Combined fictitious-sources–scattering-matrix method," J. Opt. Soc. Am. A **21**, 1417–1423 (2004).
[75]E. Moreno, D. Erni, and C. Hafner, "Modeling of discontinuities in photonic crystal waveguides with the multiple multipole method," Phys. Rev. E **66**, 036618 (2002).
[76]H.-Y. Xu and Y.-C. Lai, "Pseudospin-1 wave scattering that defies chaos *Q*-spoiling and Klein tunneling," Phys. Rev. B **99**, 235403 (2019).
[77]H.-Y. Xu and Y.-C. Lai, "Anomalous chiral edge states in spin-1 Dirac quantum dots," Phys. Rev. Res. **2**, 013062 (2020).
[78]C.-Z. Wang, H.-Y. Xu, and Y.-C. Lai, "Scattering of Dirac electrons from a skyrmion: Emergence of robust skew scattering," Phys. Rev. Res. **2**, 013247 (2020).
[79]C.-D. Han, H.-Y. Xu, and Y.-C. Lai, "Pseudospin modulation in coupled graphene systems," Phys. Rev. Res. **2**, 033406 (2020).
[80]A. Krizhevsky, I. Sutskever, and G. E. Hinton, "ImageNet classification with deep convolutional neural networks," Commun. ACM **60**, 84–90 (2017).
[81]S. Ioffe and C. Szegedy, "Batch normalization: Accelerating deep network training by reducing internal covariate shift," in *International Conference on Machine Learning* (PMLR, 2015), pp. 448–456.
[82]A. Paszke, S. Gross, F. Massa, A. Lerer, J. Bradbury, G. Chanan, T. Killeen, Z. Lin, N. Gimelshein, L. Antiga *et al.*, "PyTorch: An imperative style, high-performance deep learning library," Adv. Neural Inf. Process. Syst. **32**, 1 (2019).
[83]P. Virtanen, R. Gommers, T. E. Oliphant, M. Haberland, T. Reddy, D. Cournapeau, E. Burovski, P. Peterson, W. Weckesser, J. Bright, S. J. van der Walt, M. Brett, J. Wilson, K. J. Millman, N. Mayorov, A. R. J. Nelson, E. Jones, R. Kern, E. Larson, C. J. Carey, İ. Polat, Y. Feng, E. W. Moore, J. VanderPlas, D. Laxalde, J. Perktold, R. Cimrman, I. Henriksen, E. A. Quintero, C. R. Harris, A. M. Archibald, A. H. Ribeiro, F. Pedregosa, P. van Mulbregt, and SciPy 1.0 Contributors, "SciPy 1.0: Fundamental algorithms for scientific computing in Python," Nat. Methods **17**, 261–272 (2020).
[84]G. M. Rutter, J. Crain, N. Guisinger, T. Li, P. First, and J. Stroscio, "Scattering and interference in epitaxial graphene," Science **317**, 219–222 (2007).
[85]A. F. Young and P. Kim, "Quantum interference and Klein tunnelling in graphene heterojunctions," Nat. Phys. **5**, 222–226 (2009).
[86]F. Monticone and A. Alu, "Do cloaked objects really scatter less?," Phys. Rev. X **3**, 041005 (2013).
[87]R. Fleury, F. Monticone, and A. Alù, "Invisibility and cloaking: Origins, present, and future perspectives," Phys. Rev. Appl. **4**, 037001 (2015).
[88]R. C. Devlin, M. Khorasaninejad, W. T. Chen, J. Oh, and F. Capasso, "Broadband high-efficiency dielectric metasurfaces for the visible spectrum," Proc. Natl. Acad. Sci. U. S. A. **113**, 10473–10478 (2016).
[89]L. Verslegers, Z. Yu, Z. Ruan, P. B. Catrysse, and S. Fan, "From electromagnetically induced transparency to superscattering with a single structure: A coupled-mode theory for doubly resonant structures," Phys. Rev. Lett. **108**, 083902 (2012).
[90]D. Zhu, Z. Liu, L. Raju, A. S. Kim, and W. Cai, "Building multifunctional metasystems via algorithmic construction," ACS Nano **15**, 2318–2326 (2021).
[91]Y. Huang, Y. Shen, C. Min, and G. Veronis, "Switching photonic nanostructures between cloaking and superscattering regimes using phase-change materials [Invited]," Opt. Mater. Express **8**, 1672–1685 (2018).
[92]S. Lepeshov, A. Krasnok, and A. Alú, "Nonscattering-to-superscattering switch with phase-change materials," ACS Photonics **6**, 2126–2132 (2019).
[93]M. Farhat, C. Rockstuhl, and H. Bağcı, "A 3D tunable and multi-frequency graphene plasmonic cloak," Opt. Express **21**, 12592–12603 (2013).
[94]R. Li, X. Lin, S. Lin, X. Liu, and H. Chen, "Atomically thin spherical shell-shaped superscatterers based on a Bohr model," Nanotechnology **26**, 505201 (2015).
[95]R. Zhao, P. Wan, L. Zhou, D. Huang, H. Guo, H. Xia, and J. Du, "Electron metasurfaces in graphene," Phys. Rev. B **107**, 155404 (2023).

[96]V. N. Kotov, B. Uchoa, V. M. Pereira, F. Guinea, and A. Castro Neto, "Electron-electron interactions in graphene: Current status and perspectives," Rev. Mod. Phys. **84**, 1067–1125 (2012).
[97]J. Hofmann, E. Barnes, and S. Das Sarma, "Why does graphene behave as a weakly interacting system?," Phys. Rev. Lett. **113**, 105502 (2014).
[98]J. P. Reed, B. Uchoa, Y. I. Joe, Y. Gan, D. Casa, E. Fradkin, and P. Abbamonte, "The effective fine-structure constant of freestanding graphene measured in graphite," Science **330**, 805–808 (2010).
[99]R. R. Nair, P. Blake, A. N. Grigorenko, K. S. Novoselov, T. J. Booth, T. Stauber, N. M. Peres, and A. K. Geim, "Fine structure constant defines visual transparency of graphene," Science **320**, 1308 (2008).
[100]H. Hadipour, E. Şaşıoğlu, F. Bagherpour, C. Friedrich, S. Blügel, and I. Mertig, "Screening of long-range Coulomb interaction in graphene nanoribbons: Armchair versus zigzag edges," Phys. Rev. B **98**, 205123 (2018).
[101]O. Vafek and J. Kang, "Renormalization group study of hidden symmetry in twisted bilayer graphene with Coulomb interactions," Phys. Rev. Lett. **125**, 257602 (2020).
[102]T. J. Peltonen, R. Ojajärvi, and T. T. Heikkilä, "Mean-field theory for superconductivity in twisted bilayer graphene," Phys. Rev. B **98**, 220504 (2018).
[103]D. Boyda, V. Braguta, M. Katsnelson, and M. Ulybyshev, "Many-body effects on graphene conductivity: Quantum Monte Carlo calculations," Phys. Rev. B **94**, 085421 (2016).
[104]P. E. Trevisanutto, C. Giorgetti, L. Reining, M. Ladisa, and V. Olevano, "*Ab initio GW* many-body effects in graphene," Phys. Rev. Lett. **101**, 226405 (2008).
[105]V. J. Härkönen, R. van Leeuwen, and E. K. Gross, "Many-body Green's function theory of electrons and nuclei beyond the Born-Oppenheimer approximation," Phys. Rev. B **101**, 235153 (2020).
[106]J. Gielis, "A generic geometric transformation that unifies a wide range of natural and abstract shapes," Am. J. Bot. **90**, 333–338 (2003).